

Simulation of Active Soft Nets for Capture of Space Debris

Leone Costi and Dario Izzo ^{*}

Abstract

In this work, we propose a simulator, based on the open-source physics engine MuJoCo, for the design and control of soft robotic nets for the autonomous removal of space debris. The proposed simulator includes net dynamics, contact between the net and the debris, self-contact of the net, orbital mechanics, and a controller that can actuate thrusters on the four satellites at the corners of the net. It showcases the case of capturing Envisat, a large ESA satellite that remains in orbit as space debris following the end of its mission. This work investigates different mechanical models, which can be used to simulate the net dynamics, simulating various degrees of compliance, and different control strategies to achieve the capture of the debris, depending on the relative position of the net and the target. Unlike previous works on this topic, we do not assume that the net has been previously ballistically thrown toward the target, and we start from a relatively static configuration. The results show that a more compliant net achieve higher performance when attempting the capture of Envisat. Moreover, when paired with a sliding mode controller, soft nets are able to achieve successful capture in 100% of the tested cases, whilst also showcasing a higher effective area at contact and a higher number of contact points between net and Envisat.

Keywords: Space, LEO, Space Debris, Capture, Simulator, Soft Robotics.

1. Introduction

Satellites have moved from specialist assets to largely unseen infrastructure, supporting essential services across communications, navigation, finance, and security as mega-constellations expand at an unprecedented pace. While Europe's Galileo¹ is maturing into a civilian-controlled navigation backbone, deployments led by Starlink and other large constellation producers have placed thousands of spacecraft in orbit, reshaping expectations of continuous, low-latency, global coverage.² This abundance has made orbital availability an implicit assumption for an ever-wider range of terrestrial and spaceborne applications, precisely as its reliability faces mounting strain. The rapid growth in LEO activity is colliding with a deteriorating debris environment,³ where escalating collision risk and routine avoidance are eroding mission assurance today and threatening the long-term sustainability of key orbital

regimes.⁴ Moreover, the monitoring and control of debris is no longer sufficient to ensure safety in LEO,³ and active removal is often advised in order to lower the risk of collisions.⁵ As an example, the ESA e.deorbit mission had the purpose of de-orbiting a single large ESA-owned space debris from the LEO protected zone.⁶ Despite the cancellation of the mission, several studies were conducted on possible active debris removal concepts that could have been utilized. Active debris removal can be achieved with several robotic platforms, ranging from close approach methods such as grippers, harpoons, and nets to contact-free options such as lasers and electro-magnetic fields.^{4,7} Both rigid grippers⁸ and harpoons⁹ can result in mechanical damage to the debris, potentially breaking the debris itself into multiple pieces, worsening the problem. Soft grippers have been hypothesized as an alternative to rigid ones,¹⁰ but the low durability of state-of-the-art

^{*}All authors are part of the Advanced Concepts Team, European Space Agency, Noordwijk, Netherlands, 2201 AZ Leone.Costi@esa.int

elastomeric materials prevents them from being a valid alternative. Similarly, using contact-free options such as lasers is impractical due to significant limitations in efficiency, cost, and geopolitical risk.¹¹

Compared to the other approaches, methods based on soft nets have two main advantages: high compliance and low weight.¹² The dynamics involved have already been investigated in detail in both the deployment phase¹³ and the capture phase,¹⁴ as well as the relative control from a distance post-capture.^{15,16} Given the importance of modeling and simulation before deployment, many attempts have been performed at implementing a simulator, from the Bullet physics engine¹⁷ to Matlab.¹⁸ These two works have later been merged into a complete simulator that was verified with a parabolic flight experiment.¹⁹ Concurrently, several other simulators have been deployed, with a focus on different phases of the capture process. Some studies are centered on the variable dynamics of the debris,^{18,20} whereas others have decided to investigate the robustness of the capture phase.²¹ Moreover, *Si et al.*²² have investigated the effect of the self-contact of the net, often ignored by other studies. Finally, *Botta et al.*²³ presented a software simulation tool for modeling the ballistic capture of space debris through a tether-actuated net system with active closure control.

Although most of the research field relies on fully passive nets, active control of the four corners has been proposed as an alternative method to further improve the success rate of capture. Explored strategies of active control include maximizing the net's area at contact,²⁴ considering multiple closing actions in case of initial failure,²⁵ sub-optimal contact point,²⁶ and dynamical assessment of the target position.²⁷ Despite using active control, these studies still rely on a mother-ship to ballistically launch the net toward the target, and the control is solely used to perform small adjustments or to help the closing of the net around the debris after the contact is initiated.

In this work, we present a simulator that can reproduce the physical interaction between the net and the debris, as well as the self-contact of the net, and includes modules both for the close-loop control strategy and the effect of orbital dynamics.

Moreover, we showcase how the simulator can be used by implementing the case of the capture of Envisat.²⁸ Envisat was a European Space Agency Earth-observing satellite launched in 2002, and after losing contact in 2012, it now remains inactive in orbit around Earth as a large piece of space debris. As one of the biggest debris present in LEO, it represents a particularly challenging milestone for the field of space debris removal.²⁹

2. Material and Methods

The proposed simulator is based on the open-source physics engine MuJoCo, with added modules to implement orbital mechanics and control strategy. Fig. 1 showcases how the simulator merges the contribution of the active controller and the action of orbital dynamics, updating the applied force on all objects of the scene, in between the physical simulation steps.

[Figure 1 about here.]

Practically, additional forces \mathbf{F} are computed and added to the simulation each timestep, and can be divided as follows:

$$\mathbf{F} = \mathbf{F}_{orb} + \mathbf{F}_{con} \quad (1)$$

where \mathbf{F}_{orb} is the force acting on each point mass due to the orbital mechanics and \mathbf{F}_{con} is the thrust applied by the control strategy. Additionally, the mass of the four thrusters is also updated in between simulation steps, in order to account for the mass ejected during propulsion.

2.1. Physics Simulator

MuJoCo itself is used to simulate Envisat and the soft net. The net is modeled as $N \times M$ point masses connected in a grid-like fashion. The specific dynamics used for the connections are implemented with three different methods: Inextensible edges, Shell, and Saint-Venant solid. In Inextensible edges, the distance between connected nodes is fixed, but the nodes can act as pivots, achieving large bending behavior. Shell is similar to the previous case but with a user-defined bending stiffness that limits the local bending radius, achieved with the Shell plug-in. Conversely, Saint-Venant models the net as a Saint-Venant solid thanks to

the Elasticity plug-in, based on user-defined values of Young's Modulus, Poisson ratio, and damping. These three different models are used to simulate different mechanical behaviors. Depending on the material used in the real scenario, the net can be simulated as extensible, inextensible, but infinitely flexible, or just flexible. Additional user inputs that can be used to tune the simulation are the 3D object used as debris, its initial velocity, and the relative initial position and velocity of the net.

2.2. Orbital Mechanics

To simulate the effect of orbital mechanics, we implement the Clohessy-Wiltshire (CW) equations under the assumption of a circular reference orbit. Envisat orbits at an approximate altitude of 790 km, corresponding to a mean orbital radius $r_0 = 7,171$ km, and an angular velocity $\omega = 0.0011$ rad/s, computed from Kepler's third law. The CW equations describe the linearized relative dynamics in the Hill (or Local-Vertical Local-Horizontal) frame centered on Envisat:

$$\begin{aligned}\ddot{x} &= 3\omega^2 x + 2\omega\dot{y}, \\ \ddot{y} &= -2\omega\dot{x}, \\ \ddot{z} &= -\omega^2 z,\end{aligned}\tag{2}$$

where x , y , and z represent the relative position of the chaser with respect to Envisat in the radial, along-track, and cross-track directions, respectively. Since the net is simulated using point masses, the acceleration is computed for each mass considered as the chaser in the CW equations, and the equivalent force \mathbf{F}_{orb} is computed as follows:

$$\mathbf{F}_{orb} = m[\ddot{x}, \ddot{y}, \ddot{z}]\tag{3}$$

where m is the mass of the point mass taken into consideration. It has to be noted that almost all masses in the simulation we present are 100 g, except the four corners, which are representing the satellites that provide the active thrust, which weigh 350 kg. Despite such a mass for the satellites is far greater than what is described in the CubeSat standard,^{30,31} such values are necessary to allow for the de-orbiting of Envisat after the capture has been achieved. Considering a debris mass of 7821 kg and a target velocity change of

193 m/s,³² the total mass of utilized fuel according to Tsiolkovsky's rocket equation³³ amounts to 683.7 kg, with a specific impulse of 250 s. According to ESA's CDF study e.deorbit,³⁴ a feasible mission will have a mass fuel fraction of 51%. This leads to an initial satellite mass of 341.16 kg. However, the capturing maneuver also requires fuel. For such a reason, we have decided on a starting mass of 350 kg, and will use the simulator also to verify that the mass expelled during capture is maintained under the safety margin, so as to allow de-orbiting after capture.

2.3. Control Strategy

The control module receives the position of the net and of the target, Envisat, as input and determines the force \mathbf{F}_{con} used by the control strategy. Whereas in principle every point mass could be controlled, we have limited the control to the four heavier masses placed at the corners of the net, simulating the satellites. This is not only in agreement with the state-of-the-art literature but also represents a realistic scenario for a practical implementation. In the example presented here, the control strategy is divided into high-level and low-level control. The high-level control selects the current phase within the capture and the relative target position of the satellites, and it is implemented as a finite-state machine (see Fig. 2).

[Figure 2 about here.]

In a general initial scenario with the net not in contact with debris nor aligned to it at the start, the four satellites at the corners of the net start rotating the net whilst also maintaining an open square configuration to maximize the useful capture area of the net. Such a phase is herein called the orienting phase (see Fig. 2B). This is achieved by considering the projection of the satellites onto a plane defined by the first two principal components of their position. Such principal components are extracted using a PCA, and the angle between the normal to the plane defined by those components and the vector from the center of the net to the center of the target is defined as the leftover angle. In the orienting phase, the target position of the satellites is computed by a rotation of the current position that corresponds to a leftover angle of 0, whilst maintaining a stretched

configuration. When the leftover angle is below a given threshold, which has been set to $36\ deg$ in this work, and the four satellites' projections cover at least 80% of the area of the fully stretched configuration, the finite state machine switches to the approaching phase, where the target position is similar to the previous phase, but with an added component, defined as the vector from the center of the net to the center of the target (see Fig. 2C). Lastly, upon contact, the satellites' centroid is determined by their mean position, and they are propelled toward such a centroid to properly envelop the target (see Fig. 2D). If the capture fails, the net detects it upon the absence of external contact and starts opening up and aligning with the target, preparing itself for another attempt.

After the high-level control selects the target position of the four corners, the low-level control is implemented either using PID or Slide Mode Control (SMC). The PID controller is implemented as follows:

$$\mathbf{F}_{\text{con}} = K_p e + K_i \int_0^T e \, dt + K_d \dot{e} \quad (4)$$

where $e = q_{\text{tar}} - q$, $q = [x, y, z]$, the index *tar* refers to the target positions determined by the high-level control, T is the current time, and K_p , K_i , and K_d are the proportional, integral, and derivative gains, respectively. For this study, these parameters are set to $K_p = 10^{-2}$, $K_i = 10^{-4}$, and $K_d = 10^{-3}$. Such values have been empirically tuned to achieve a quick response, thus higher maneuverability of the net, whilst maintaining the thrust within a feasible range.

[Figure 3 about here.]

Alternatively, we employ SMC to drive the system toward the target point. SMC is a nonlinear control technique known for its robustness in the presence of modeling uncertainties and external disturbances.³⁵ This robustness arises from the use of a discontinuous, or rapidly varying, control term that enforces the system's trajectory to "slide" along a predetermined manifold in the state space, known as the sliding surface. In this approach, the control force \mathbf{F}_{con} is defined as:

$$\mathbf{F}_{\text{con}} = \mathbf{F}_{\text{eq}} + \mathbf{F}_{\text{sw}} \quad (5)$$

where \mathbf{F}_{eq} and \mathbf{F}_{sw} are the equivalent control and switching terms, respectively. The former term

dictates motion along the sliding manifold toward the target state, while the latter represents a nonlinear switching control that engages whenever the trajectory departs from the manifold, enforcing convergence back onto the surface. The switching term is defined as follows:

$$\begin{cases} \mathbf{F}_{\text{sw}} = -K \tanh\left(\frac{s}{\sigma}\right) \\ s = -(\dot{e} + \lambda e) \end{cases} \quad (6)$$

where s is the manifold, or sliding surface, and the parameters λ , K , and σ are user-defined control gains that shape the system's convergence behavior and robustness. Specifically, λ determines the slope of the sliding surface, K sets the magnitude of the switching control term, and σ smooths the discontinuity in the tanh function to mitigate chattering effects. Note that we maintain the definition of the error as $e = q_{\text{tar}} - q$ for consistency with the PID controller (see Eq. 4), rather than $e = q - q_{\text{tar}}$, which is most commonly used in SMC formulations.^{36,37} The term \mathbf{F}_{eq} is then derived by imposing $\dot{s} = 0$, leading to:

$$\mathbf{F}_{\text{eq}} = m\ddot{q} - m\ddot{q}_{\text{tar}} - m\lambda\dot{e} \quad (7)$$

which finally results in the control law:

$$\mathbf{F}_{\text{con}} = m\ddot{q} - m\ddot{q}_{\text{tar}} - m\lambda\dot{e} - K \tanh\left(\frac{\dot{e} + \lambda e}{\sigma}\right) \quad (8)$$

with positions, velocities, and accelerations both of the target and point masses directly accessible via MuJoCo at each timestep. This formulation enables fast convergence to the desired state while maintaining stability under uncertainties and disturbances, which makes SMC particularly suitable for high-precision or safety-critical tasks. For this study, these parameters are set to $\lambda = 1 \cdot 10^{-2}$, $K = 3 \cdot 10^{-2}$, and $\sigma = 10^{-2}$. In particular, λ has been selected identical to K_p for the PID controller, as both terms govern the aggressiveness of error correction: λ determines the exponential convergence rate of the tracking error on the sliding surface, in the same way that K_p influences the decay rate of the error in a proportional control scheme.

Regardless of the low-level control method implemented, the maximum force that can be delivered by the thrusters has been limited to $20\ N$. After the thrust \mathbf{F}_{con} has been computed, the mass

of each one of the four satellites is updated to account for the mass that was ejected to achieve such a thrust. Based on Tsiolkovsky's rocket equation,³³ the mass of each satellite is computed as:

$$m = m_0 - \frac{1}{I_{sp} g_0} \int_0^T \mathbf{F}_{\text{con}}(t) dt \quad (9)$$

where m_0 is the initial mass of each satellite, T is the current time, I_{sp} is the specific impulse and $g_0 = 9.80665 \text{ m/s}^2$ is the standard acceleration due to gravity at Earth's surface. In this study, since the maximum thrust is set to 20 N , the specific impulse is set at $I_{sp} = 250 \text{ s}$ to model a representative chemical propulsion system.

2.4. Experimental protocol

To evaluate the performance of the simulation tool, we have tested all the possible formulations for the net and both low-level control methods. We have performed a set of simulations to investigate all possible orientations of the net relative to Envisat, sampling 200 starting points uniformly from a sphere of radius 5 m centered on Envisat, while maintaining the starting absolute orientation of the net constant. In all cases, the integration step is kept constant at 20 ms and simulations are run until the capture of Envisat. The captured state is reached when the net envelopes Envisat, with contact between Envisat and the net, the four satellites within 8 m of each other, and the difference between the barycenter velocities of the net and Envisat being within 0.1 m/s . Such conditions need to be met continuously for at least 200 simulation steps. Unlike other studies on the topic, we do not assume that the net is already traveling toward the target, or that it is correctly oriented. In particular, the net is always initialized with the same absolute orientation and 0 relative velocity with respect to Envisat. For the Shell and Saint-Venant formulations, we have selected a Young's modulus of 10 kPa , a Poisson ratio of 0.3, and a damping coefficient of 10^{-2} .

3. Results

The investigation herein reported has been performed using a 10×10 point mass grid and an integration step of 20 ms . Under these conditions, the simulation tool is able to run at a fre-

quency above 50 Hz on a single CPU. This allows the simulator to run in effectively real time, unlike previous studies, which needed much longer simulation times.²³ The dynamics of the capture greatly differ depending on the mechanical characteristics and the different models. Fig. 3 shows the three different phases of Envisat's capture in the different tested methodologies. It can be noticed that the controller type greatly affects the capture time and the shape of the net. In the case of SMC, the net oscillates while trying to maintain the desired opening area throughout the motion. This happens at the cost of reorientation speed, with the SMC controller taking much longer than the PID to start to accelerate toward the target. Conversely, the PID controller moves the corners more abruptly, resulting in a faster, but less organized reorientation of the net, particularly during the capture phase. Concerning the modeling of the net, the Shell formulation results in a visibly lower local bending radius, as expected by the presence of a bending stiffness.

For a more in-depth analysis, Fig. 4 showcases the trajectory taken by the four corners during capture under the Saint-Venant formulation with an SMC controller.

[Figure 4 about here.]

The results show a successful example of the capture of Envisat in just under 500 s . Whilst Fig. 4A-C show the trajectory in space both of the target and of the corners of the net, Fig. 4D shows the time-series of the z position. Both the net and the target start with no relative velocity between them, and the net starts reorienting itself and moving toward Envisat until capture. A successful capture can be verified by Envisat moving together with the net, and from the applied thrust reaching 0. As shown in Fig. 4E, the fuel mass needed for this maneuver is roughly 0.5 kg per satellite, for a total of 2 kg . This is well within the margin of extra fuel added on top of the amount needed for Envisat's de-orbiting, thus allowing such a task to be completed after capture.

However, metrics such as the time needed to achieve a capture or the success rate heavily depend on the relative start position between Envisat and the net. Fig. 5 shows all the tested cases when investigating a wide range of starting conditions,

divided by type of controller and model used to represent the net. Additionally, Table 1 summarizes the capture percentage, the fraction of all tested starting positions that resulted in a capture within 600 s.

[Figure 5 about here.]

[Table 1 about here.]

In general, PID performs worse than SMC across all net models. This can be explained by the greater resilience to nonlinearities that SMC shows, thanks to the switching term. This comprehensive view confirms what has been observed for a specific case in Fig. 3: SMC is much slower than PID, especially when approaching Envisat from above and from the sides. This difference is less visible when the net starts below Envisat. This is probably due to the presence of Envisat's solar panel. Moreover, SMC also achieves a higher effective area of the net upon contact, indicated by the marker size in Fig. 5, potentially achieving an overall higher success rate. For both controllers, the results indicate that more compliance leads to a higher success rate, with the Saint-Venant formulation reaching up to 100% accuracy.

A secondary metric we are interested in is the amount of fuel that is needed for the maneuver. A low amount of expelled material is fundamental to achieve capture with enough fuel mass left to perform the de-orbiting. The mass can be computed using Eq. 9, and it is shown in Fig. 6 as a function of the starting position of the net with respect to Envisat, the mechanical formulation of the net, and the controller. Note that only points corresponding to successful captures are plotted.

[Figure 6 about here.]

In general, all combinations of controller and net models show a similar range of needed fuel mass, up to a few tens of kg , less than the $683.7\,kg$ needed for the de-orbiting (see Section 2.2), and well within our initially estimated margin. Another metric that can be estimated is the number of contact points. All combinations show a wide range of values with high variability depending on the starting position of the net. Noticeably, the SMC controller generally achieves a higher number of contact points with respect to the PID counterparts.

Lastly, more data about the kinematics and dynamics can be plotted as a function of the net model and the controller, as shown in Fig. 7.

[Figure 7 about here.]

Concerning the dynamics, it can be seen that the applied thrust by the satellites is mainly dependent on the control strategy. On one hand, the PID controller outputs a small range of desired thrusts. On the other hand, SMC is characterized by a much wider range of values. More in detail, the average thrust of SMC is roughly one order of magnitude greater than that of PID. This is probably due to a frequent activation of the switching term, which can be caused by the contact nonlinearities present in the system. Concerning internal stresses (Fig. 6B), they are mainly affected by the net mechanical model implemented. The Saint-Venant model showcases much higher internal forces with respect to the shell model. However, internal forces are maintained in the order of tens of N , which is bearable for an extremely wide range of materials. Lastly, concerning the kinematics (Fig. 6C-D), all combinations of net mechanical model and controller appear to showcase similar distributions. In the case of acceleration, it can be seen how the higher forces observed in Fig. 6A lead to heavier tails with higher accelerations in the case of SMC. Conversely, the velocity distributions are much more similar.

Overall, the kinematics and dynamics of the simulation are mainly affected by the choice of the controller, but both controllers lead to values that are well within feasible technical implementation, including material properties, desired thrusts, and achieved kinematics.

4. Conclusion

This work proposes a simulator for the investigation of debris capture in space using highly compliant soft active nets. We demonstrate the application by simulating the capture of Envisat, implementing three different formulations for the mechanical behavior of the controller, and two different types of controllers, and investigating a wide range of initial relative positions between Envisat and the net.

The results show that increased compliance often results in a higher capture success rate, but

also that an SMC outperforms PID as a controller. The former phenomenon can be explained by more compliant nets that better conform to the Envisat shape, thus achieving a better contact and a more likely capture. Conversely, the latter highlights how the greater resilience of SMC to the nonlinearities of the simulated problem results in a higher success rate, higher effective area, and number of contact points, at the expense of the capturing time.

Nevertheless, whereas in principle Envisat represents one of the hardest debris to de-orbit, given its size and weight, further studies on different types of debris are needed to investigate how both the mechanical properties of the net and the implemented controller can be improved based on the size, mass, and geometry of the target, as well as its orbit. Moreover, both implemented controllers' performance is highly dependent on the parameters. As an example, when changing the starting distance from 5 m to 10 m without changing the parameters, the success rate drops to 93.5%. Hence, we endorse further studies on the characterization of how the controller's parameters can be optimized as a function of both the target and the mechanical model of the net.

In summary, we have proposed a simulator that can be used to investigate soft active nets for space debris capture, and have showcased the case of Envisat as a demonstration, achieving 100% capture success when starting the simulations 5 m from it. We hope that this work will pave the way for further technical development of active soft nets as a solution for space debris removal and orbital robotics.

Data Availability

The source code used to run the simulations and obtained results can be found at https://gitlab.com/EuropeanSpaceAgency/space_net

Author Disclosure Statement

The authors declare no conflicts of interest.

References

- ¹ V. Oehler, H. L. Trautenberg, J. Krueger, T. Rang, F. Luongo, J. Boyereo, J. Hahn, and D. Blonski, "Galileo system design & performance," in *Proceedings of the 19th International Technical Meeting of the Satellite Division of The Institute of Navigation (ION GNSS 2006)*, pp. 492–503, 2006.
- ² F. Michel, M. Trevisan, D. Giordano, and O. Bonaventure, "A first look at starlink performance," in *Proceedings of the 22nd ACM Internet Measurement Conference*, pp. 130–136, 2022.
- ³ A. Dhinakaran, S. Nadaraja Pillai, V. Shahul Hameed, and S. B. Priya, "Review on orbital debris mitigation: Techniques for effective tracking, monitoring, and removal," nov 2025.
- ⁴ M. Bigdeli, R. Srivastava, and M. Scaraggi, "Mechanics of space debris removal: A review," *Aerospace*, vol. 12, no. 4, p. 277, 2025.
- ⁵ J.-C. Liou, "An active debris removal parametric study for leo environment remediation," *Advances in space research*, vol. 47, no. 11, pp. 1865–1876, 2011.
- ⁶ R. Biesbroek, L. Innocenti, A. Wolahan, and S. M. Serrano, "e. deorbit-esa's active debris removal mission," in *Proceedings of the 7th European conference on space debris*, vol. 10, ESA Space Debris Office Darmstadt, Germany, 2017.
- ⁷ M. Arshad, M. C. Bazzocchi, and F. Hussain, "Emerging strategies in close proximity operations for space debris removal: A review," mar 2025.
- ⁸ A. Dawood, A. Sarosh, M. Talha, and W. A. Khan, "On the Possible Utilization of an End-Effectuator Mechanism for Space Debris Remediation in Low Earth Orbit," in *Proceedings of the First International Conference on Aeronautical Sciences, Engineering and Technology*, pp. 279–286, Springer Nature Singapore, 2024.
- ⁹ W. Zhao, Z. Pang, Z. Zhao, Z. Du, and W. Zhu, "A Simulation and an Experimental Study of Space Harpoon Low-Velocity Impact, Anchored Debris," *Materials*, vol. 15, jul 2022.
- ¹⁰ F. Ruiz, B. Arrue, and A. Ollero, "Thermally-resilient soft gripper for on-orbit operations,"

in 2024 IEEE/RSJ International Conference on Intelligent Robots and Systems (IROS), pp. 14050–14055, IEEE, 2024.

¹¹ C. R. Phipps, K. L. Baker, S. B. Libby, D. A. Liedahl, S. S. Olivier, L. D. Pleasance, A. Rubenchik, J. E. Trebes, E. V. George, B. Marcovici, *et al.*, “Removing orbital debris with lasers,” *Advances in Space research*, vol. 49, no. 9, pp. 1283–1300, 2012.

¹² E. M. Botta, I. Sharf, and A. K. Misra, “Simulation of tether-nets for capture of space debris and small asteroids,” *Acta Astronautica*, vol. 155, pp. 448–461, 2019.

¹³ E. M. Botta, I. Sharf, and A. K. Misra, “Energy and momentum analysis of the deployment dynamics of nets in space,” *Acta Astronautica*, vol. 140, pp. 554–564, 2017.

¹⁴ E. M. Botta, I. Sharf, and A. K. Misra, “Contact dynamics modeling and simulation of tether nets for space-debris capture,” *Journal of Guidance, Control, and Dynamics*, vol. 40, no. 1, pp. 110–123, 2017.

¹⁵ L. Field, “MODELING, SIMULATION, AND CONTROL OF TETHERED SPACE DEBRIS,” tech. rep., 2022.

¹⁶ L. Field and E. M. Botta, “Relative Distance Control of Uncooperative Tethered Debris,” *Journal of the Astronautical Sciences*, vol. 70, dec 2023.

¹⁷ K. Wormnes, J. H. de Jong, H. Krag, and G. Visentin, “Throw-nets and tethers for robust space debris capture,” in *International Astronautical Congress*, 2013.

¹⁸ R. Benvenuto, S. Salvi, and M. Lavagna, “Dynamics analysis and gnc design of flexible systems for space debris active removal,” *Acta Astronautica*, vol. 110, pp. 247–265, 2015.

¹⁹ L. Cercós, R. Stefanescu, A. Medina, R. Benvenuto, M. Lavagna, I. González, N. Rodríguez, K. Wormnes, *et al.*, “Validation of a net active debris removal simulator within parabolic flight experiment,” in *12th International Symposium on Artificial Intelligence Robotics and Automation in Space (i-SAIRAS)*, 2014.

²⁰ M. Shan, J. Guo, and E. Gill, “Contact dynamics on net capturing of tumbling space debris,” *Journal of Guidance, Control, and Dynamics*, vol. 41, no. 9, pp. 2063–2072, 2018.

²¹ M. Shan, J. Guo, and E. Gill, “An analysis of the flexibility modeling of a net for space debris removal,” *Advances in Space Research*, vol. 65, no. 3, pp. 1083–1094, 2020.

²² J. Si, Z. Pang, Z. Du, and C. Cheng, “Dynamics modeling and simulation of self-collision of tether-net for space debris removal,” *Advances in Space Research*, vol. 64, no. 9, pp. 1675–1687, 2019.

²³ E. M. Botta, C. Miles, and I. Sharf, “Simulation and tension control of a tether-actuated closing mechanism for net-based capture of space debris,” *Acta Astronautica*, vol. 174, pp. 347–358, 2020.

²⁴ M. Ru, Y. Zhan, B. Cheng, and Y. Zhang, “Capture dynamics and control of a flexible net for space debris removal,” *Aerospace*, vol. 9, no. 6, p. 299, 2022.

²⁵ Y. Zhao, P. Huang, and F. Zhang, “Capture dynamics and net closing control for tethered space net robot,” *Journal of Guidance, Control, and Dynamics*, vol. 42, no. 1, pp. 199–208, 2019.

²⁶ Y. Zhao, F. Zhang, and P. Huang, “Capture dynamics and control of tethered space net robot for space debris capturing in unideal capture case,” *Journal of the Franklin Institute*, vol. 357, no. 17, pp. 12019–12036, 2020.

²⁷ Y. Zhao, F. Zhang, and P. Huang, “Dynamic closing point determination for space debris capturing via tethered space net robot,” *IEEE transactions on aerospace and electronic systems*, vol. 58, no. 5, pp. 4251–4260, 2022.

²⁸ J. Louet and S. Bruzzi, “Envisat mission and system,” in *IEEE 1999 International Geoscience and Remote Sensing Symposium. IGARSS’99 (Cat. No. 99CH36293)*, vol. 3, pp. 1680–1682, IEEE, 1999.

²⁹ S. Estable, C. Pruvost, E. Ferreira, J. Telaar, M. Fruhnert, C. Imhof, T. Rybus, G. Peckover, R. Lucas, R. Ahmed, *et al.*, “Capturing and deorbiting envisat with an airbus spacetug. results from the esa e. deorbit consolidation phase study,” *Journal of Space Safety Engineering*, vol. 7, no. 1, pp. 52–66, 2020.

³⁰ H. Heidt, J. Puig-Suari, A. Moore, S. Nakasuka, and R. Twiggs, “Cubesat: A new generation of picosatellite for education and industry low-cost space experimentation,” 2000.

³¹ T. Villela, C. A. Costa, A. M. Brandão, F. T. Bueno, and R. Leonardi, “Towards the thousandth cubesat: A statistical overview,” *International Journal of Aerospace Engineering*, vol. 2019, no. 1, p. 5063145, 2019.

³² S. Tonetti, S. Cornara, M. Faenza, O. Verberne, T. Langener, and G. Vicario de Miguel, “Active debris removal and space debris mitigation using hybrid propulsion solutions,” in *Stardust Final Conference: Advances in Asteroids and Space Debris Engineering and Science*, pp. 163–180, Springer, 2018.

³³ K. Tsiolkovsky, “Reactive flying machines,” *Izdatel’stvo Akademii Nauk SSSR: Moscow, Russia*, 1954.

³⁴ M. Bandecchi, “e.deorbit, cdf study report: Cdf-135(c),” tech. rep., ESA, 9 2012.

³⁵ V. Utkin, “Variable structure systems with sliding modes,” *IEEE Transactions on Automatic control*, vol. 22, no. 2, pp. 212–222, 2003.

³⁶ C. Edwards and S. K. Spurgeon, *Sliding mode control: theory and applications*. CRC press, 1998.

³⁷ Y. Shtessel, C. Edwards, L. Fridman, A. Levant, *et al.*, *Sliding mode control and observation*, vol. 10. Springer, 2014.

List of Figures

1	Overview of the simulation tool's workflow. After an initial scene initialization, both the controller and the orbital dynamics modules update the force applied to the massive bodies in the simulation between every step.	11
2	Schematics of the (A) finite-state machine representing the high-level control for the capture of space debris and of the three implemented states: (B) the orienting phase, (C) the approaching phase, and (D) the capture phase.	12
3	The three phases of the capture of Envisat as a function of the net mechanical model and the controller used: (A) Inextensible edges and PID, (B) Shell and PID, (C) Saint-Venant solid and PID, (D) Inextensible edges and SMC, (E), Shell and SMC (F) Saint-Venant solid and SMC. The starting position of all cases is the same, and the starting relative velocity between the net and Envisat is 0.	13
4	Trajectories of the four satellites with respect to the target: (A) isometric view, projection on the (B) xy plane and (C) xz plane, and (D) z position as a function of time. Data about the thrusters include: (E) mass of the satellites at the corners of the net and (F) thrust generated by each satellite as a function of time.	14
5	Time needed to achieve capture as a function of the starting positions of the for each control modality and the model used to characterize the net: (A) Inextensible edges and PID, (B) Shell and PID, (C) Saint-Venant solid and PID, (D) Inextensible edges and SMC, (E), Shell and SMC (F) Saint-Venant solid and SMC. The size of the marker is proportional to the effective area of the net upon contact with the target. The effective area is computed by the area between the projections of the four corners onto a plane perpendicular to the vector between the center of the net and the target.	15
6	Fuel mass required by the manouver as a function of the starting positions of the for each control modality and the model used to characterize the net: (A) Inextensible edges and PID, (B) Shell and PID, (C) Saint-Venant solid and PID, (D) Inextensible edges and SMC, (E), Shell and SMC (F) Saint-Venant solid and SMC. The size of the marker is proportional to the number of contact points between the net and Envisat after capture is achieved. The contact points are computed by the number of point masses in contact with Envisat when the capture is detected.	16
7	Quantitative data: (A) net internal forces, (B) applied thrust, (C) point-masses velocities, and (D) point-masses accelerations. Plots are in logarithmic scale above a selected threshold, indicated by the gray dashed line.	17

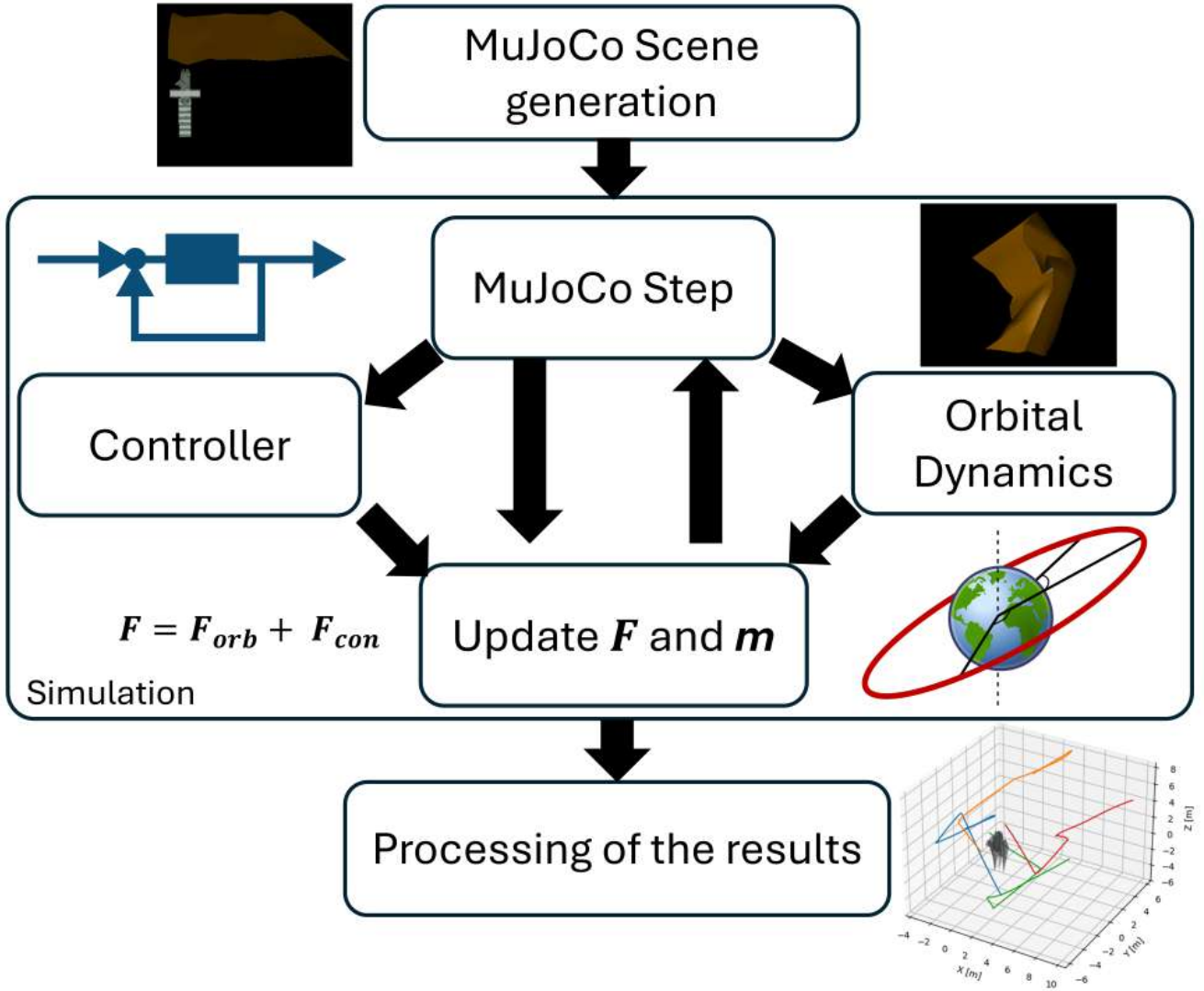


Figure 1. Overview of the simulation tool's workflow. After an initial scene initialization, both the controller and the orbital dynamics modules update the force applied to the massive bodies in the simulation between every step.

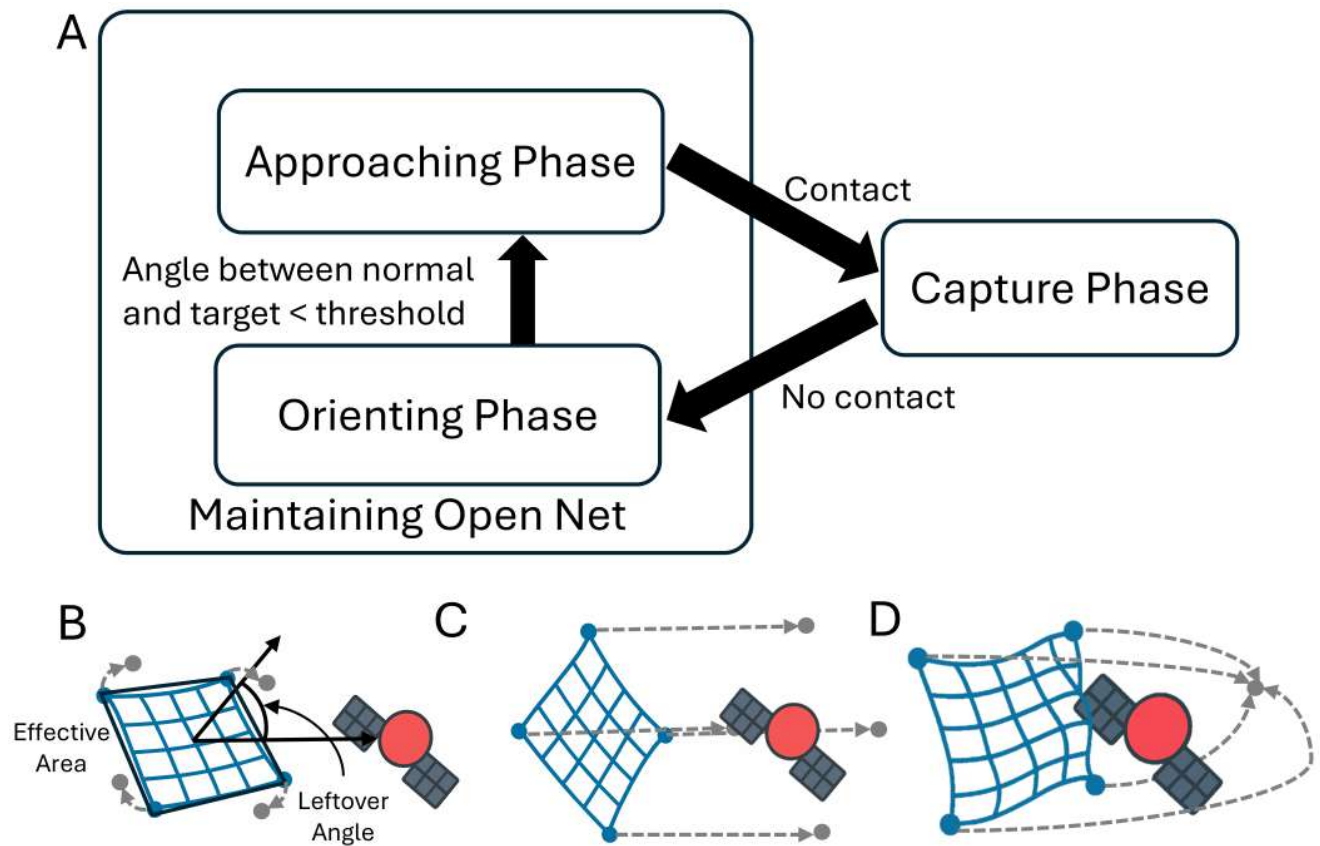


Figure 2. Schematics of the (A) finite-state machine representing the high-level control for the capture of space debris and of the three implemented states: (B) the orienting phase, (C) the approaching phase, and (D) the capture phase.

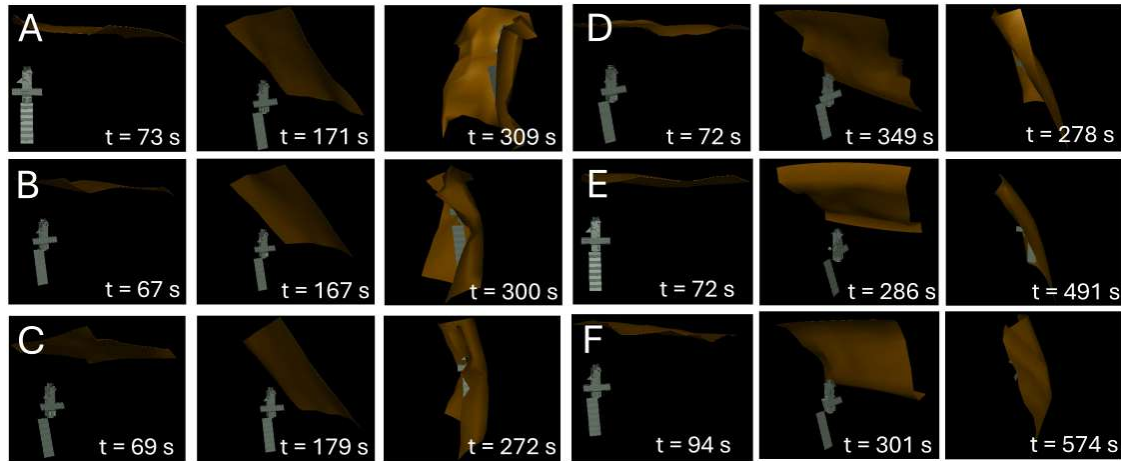


Figure 3. The three phases of the capture of Envisat as a function of the net mechanical model and the controller used: (A) Inextensible edges and PID, (B) Shell and PID, (C) Saint-Venant solid and PID, (D) Inextensible edges and SMC, (E), Shell and SMC (F) Saint-Venant solid and SMC. The starting position of all cases is the same, and the starting relative velocity between the net and Envisat is 0.

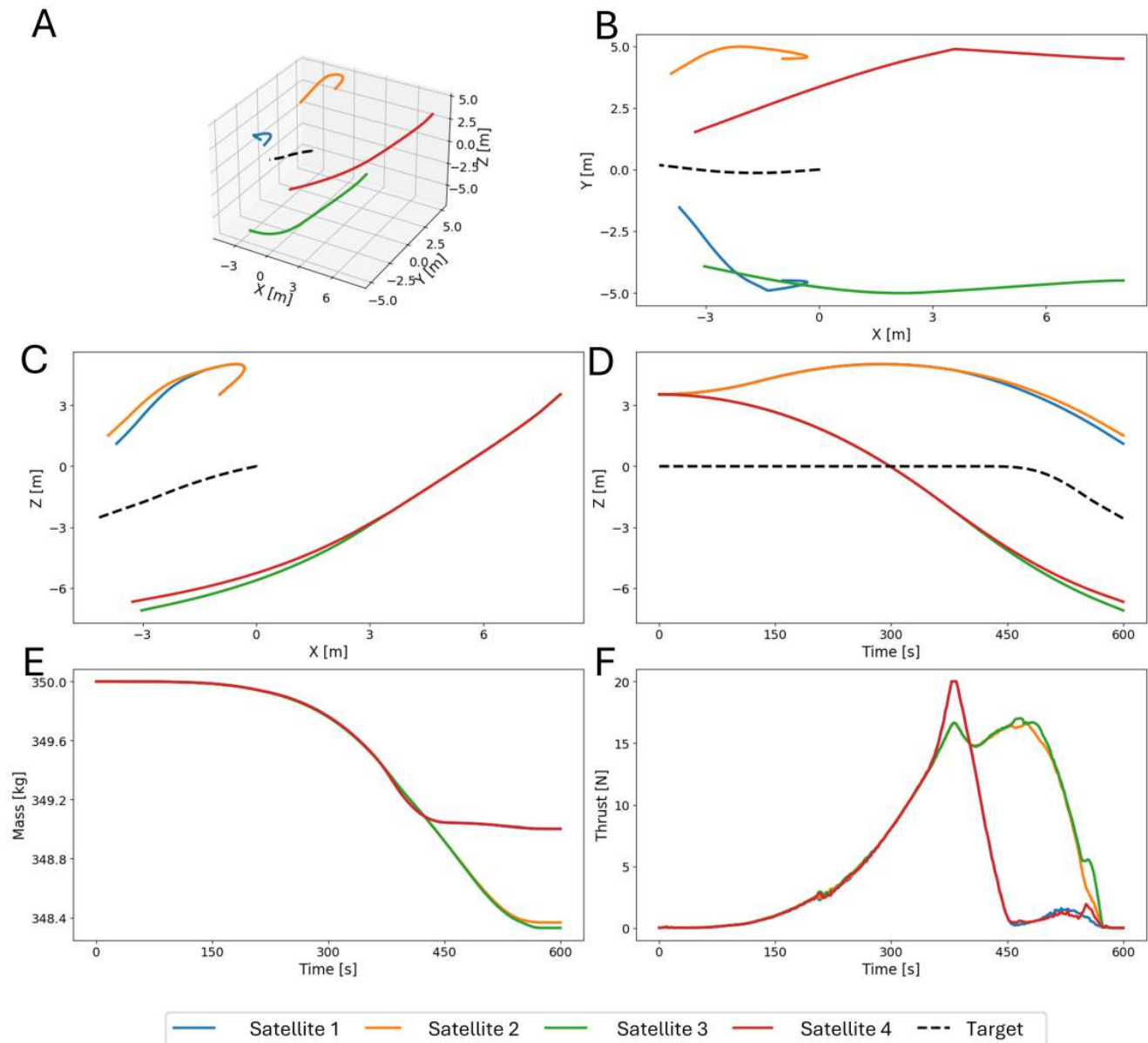


Figure 4. Trajectories of the four satellites with respect to the target: (A) isometric view, projection on the (B) xy plane and (C) xz plane, and (D) z position as a function of time. Data about the thrusters include: (E) mass of the satellites at the corners of the net and (F) thrust generated by each satellite as a function of time.

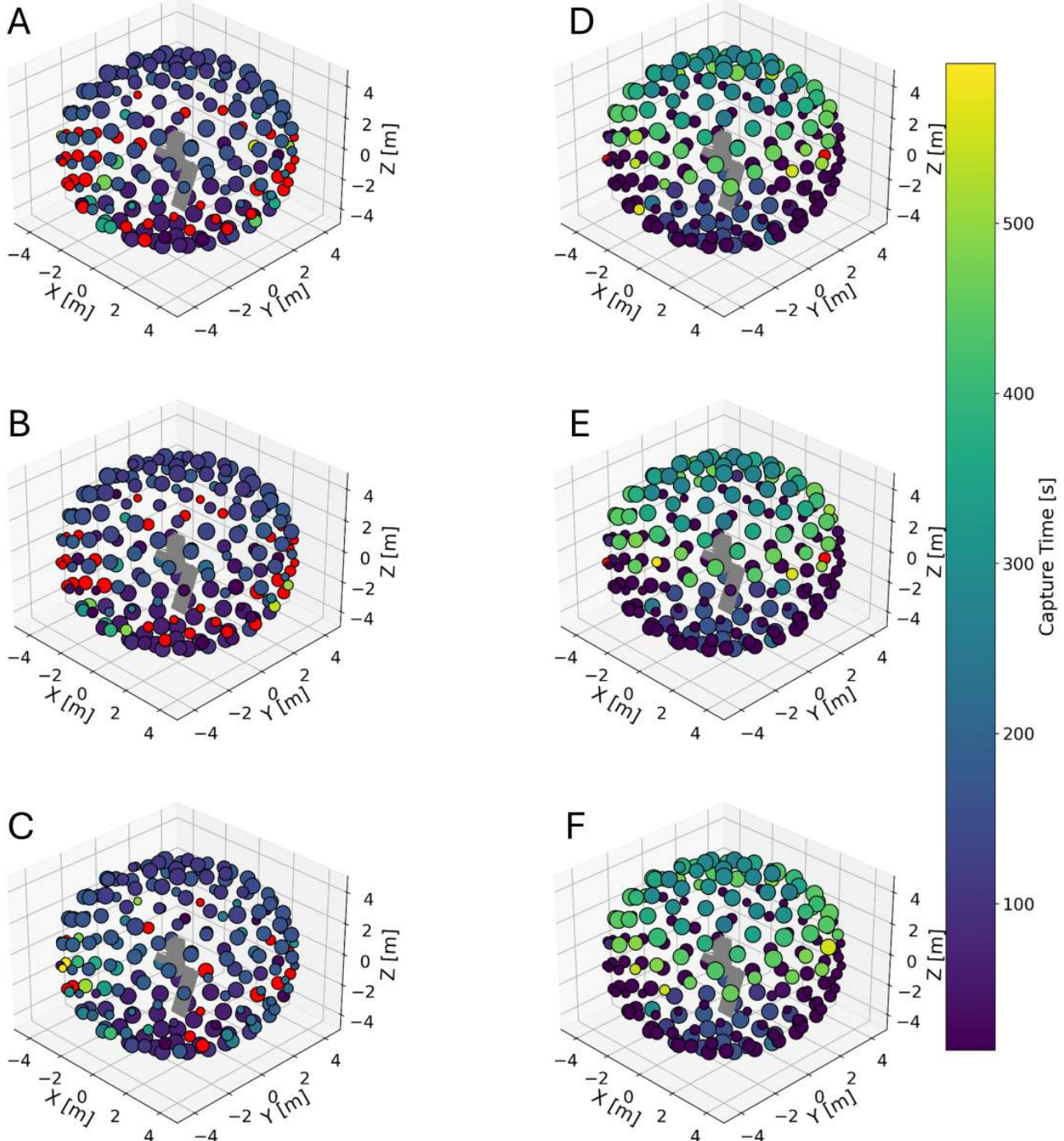


Figure 5. Time needed to achieve capture as a function of the starting positions of the for each control modality and the model used to characterize the net: (A) Inextensible edges and PID, (B) Shell and PID, (C) Saint-Venant solid and PID, (D) Inextensible edges and SMC, (E) Shell and SMC (F) Saint-Venant solid and SMC. The size of the marker is proportional to the effective area of the net upon contact with the target. The effective area is computed by the area between the projections of the four corners onto a plane perpendicular to the vector between the center of the net and the target.

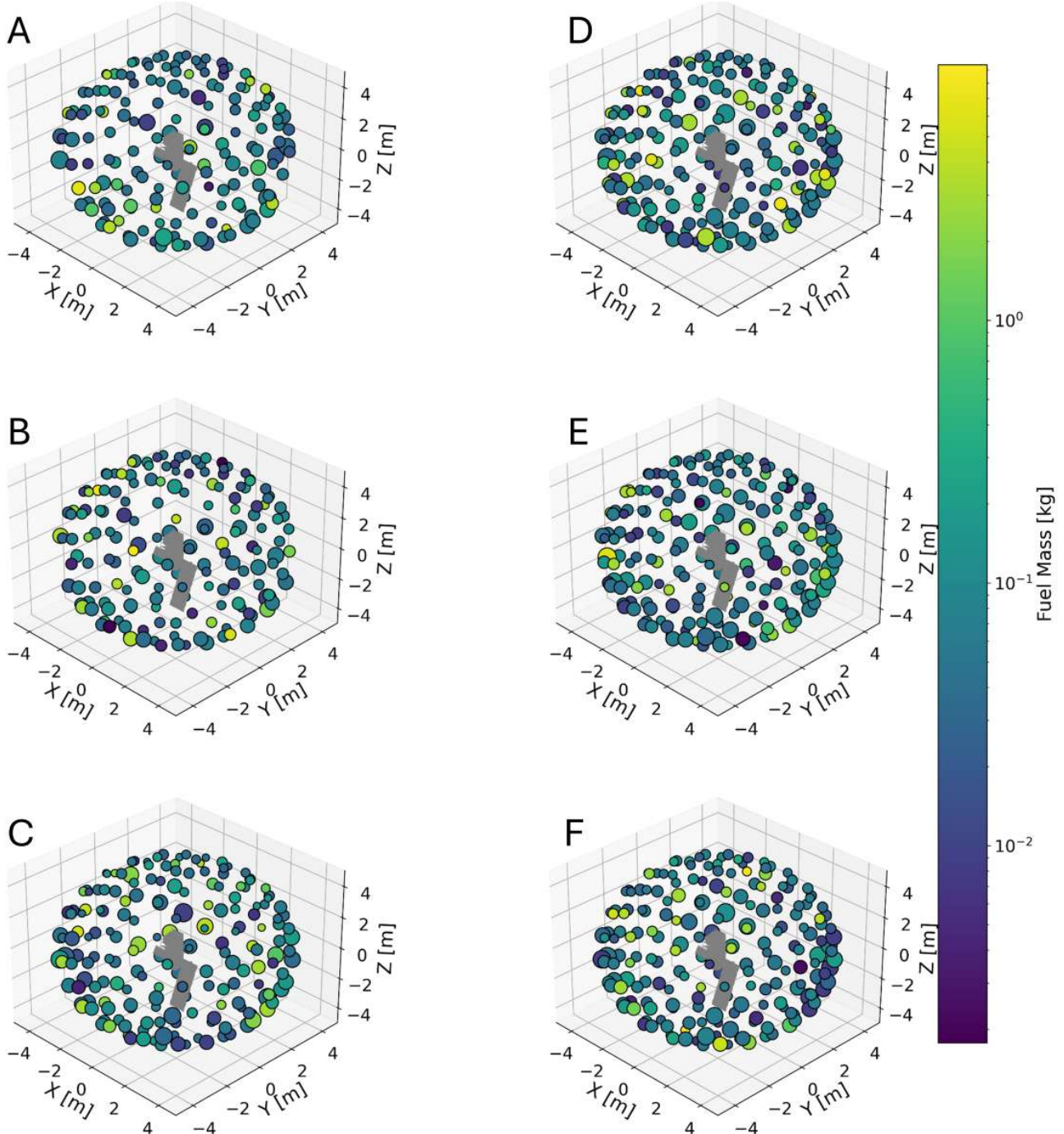


Figure 6. Fuel mass required by the manouever as a function of the starting positions of the for each control modality and the model used to characterize the net: (A) Inextensible edges and PID, (B) Shell and PID, (C) Saint-Venant solid and PID, (D) Inextensible edges and SMC, (E) Shell and SMC (F) Saint-Venant solid and SMC. The size of the marker is proportional to the number of contact points between the net and Envisat after capture is achieved. The contact points are computed by the number of point masses in contact with Envisat when the capture is detected.

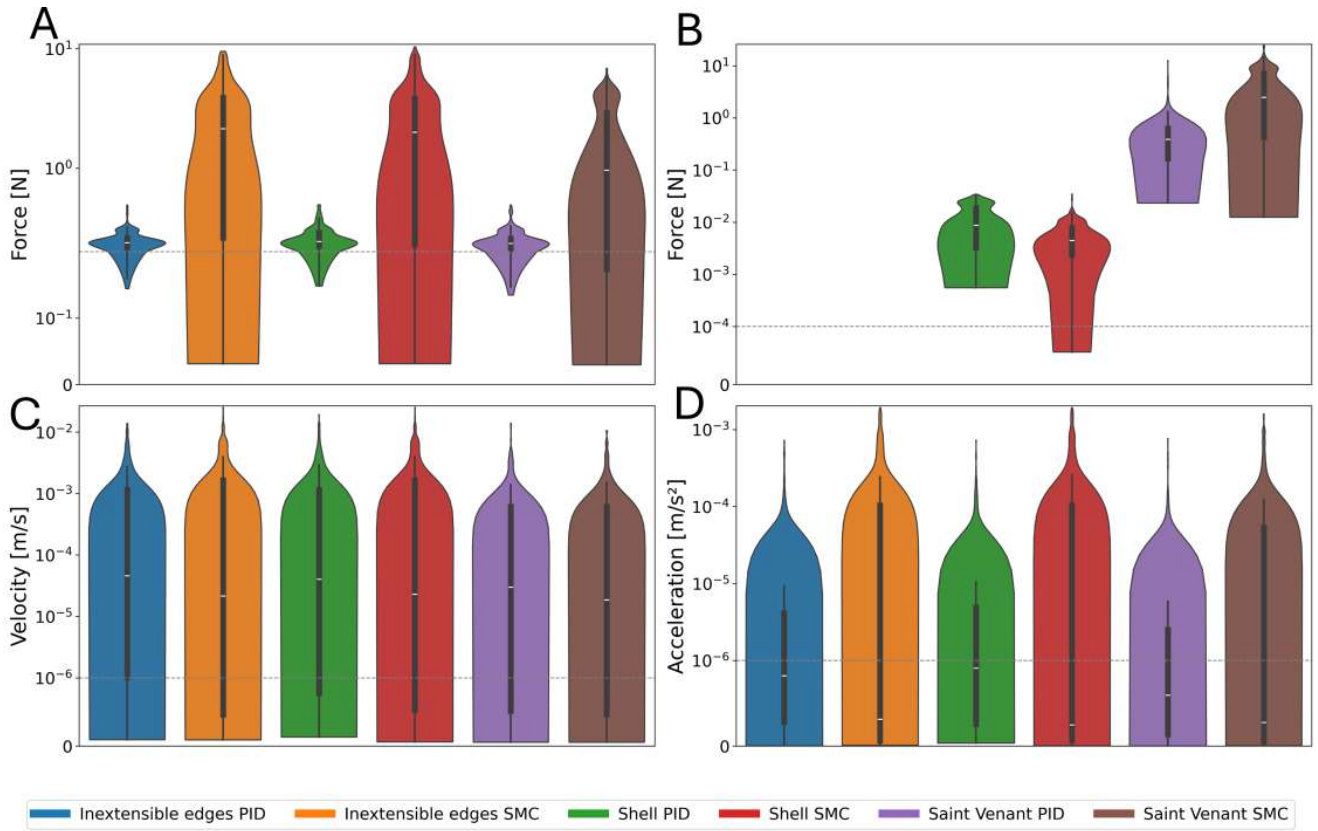


Figure 7. Quantitative data: (A) net internal forces, (B) applied thrust, (C) point-masses velocities, and (D) point-masses accelerations. Plots are in logarithmic scale above a selected threshold, indicated by the gray dashed line.

List of Tables

1	Capture percentage as a function of the control modality and the model used to characterize the net.	19
---	--	----

	Inextensible edges	Shell	Saint-Venant
PID	88.5%	86.5%	93.5%
SMC	99.5%	99.5%	100.0%

Table 1. Capture percentage as a function of the control modality and the model used to characterize the net.